Peer-reviewed version available at *Entropy* **2020**, *22*, 431; doi:10.3390/e22040431

Article

Dynamic Shear Deformation of a Precipitation Hardened $Al_{0.7}CoCrFeNi$ Eutectic High-Entropy Alloy Using Hat-Shaped Specimen Geometry

Bharat Gwalani [1,*,#], Tianhao Wang [1,#], Abhinav Jagetia [1], Sindhura Gangireddy [1], Saideep Muskeri[1], Sundeep Mukherjee [1], J. T. Lloyd [3], Rajarshi Banerjee [1,2] and Rajiv S. Mishra [1,2,*]

[1] Department of Materials Science and Engineering, University of North Texas, Denton, TX 76207 USA
[2] Advanced Materials and Manufacturing Processes Institute, University of North Texas, Denton, TX 76207 USA
[3] U.S. Army Research Laboratory, Aberdeen Proving Ground, MD, 21005, US
* Correspondence: bharatgwalani@my.unt.edu; rajiv.mishra@unt.edu
# Current Address: Pacific Northwest National Laboratory, Richland WA, USA

Abstract: Lamellar eutectic structure of $Al_{0.7}CoCrFeNi$ high-entropy alloy (HEA) is emerging as a promising candidate for structural applications because of its high strength-ductility combination. The alloy consists of a fine-scale lamellar *fcc*+B2 microstructure with high flow stresses >1500 MPa under quasi-static conditions. The response to shear loading was not investigated so far. This is the first report on the shear deformation of a eutectic structured HEA and effect of precipitation on shear deformation. The dynamic shear response (DSR) of the eutectic HEA was examined in two microstructural conditions, with and without the presence of $L1_2$ precipitates. A split-Hopkinson pressure bar (SHPB) was used to compress the hat-shaped specimens to study the local DSR of the alloy. The adiabatic shear bands (ASBs) in two different microstructural conditions were characterized after deformation at dynamic strain rates. The adiabatic shear localization occurs at low strains for the high strength material, and the eutectic microstructure does not delay cracking. The width of ASBs and the extent of plastic deformation around them has been correlated with the rate of straining. Dynamic recrystallization within ASBs and profuse twinning around it was observed. Local mechanical response of individual lamellae before and after shear deformation was examined using nano-indentation.

Keywords: Eutectic high-entropy alloy; Dynamic shear deformation; Split-Hopkinson pressure bar test; Hat-shaped specimen; Nano-indentation

1. Introduction

Lamellar structures exist widely in various metallic materials such as: A356 aluminum alloy (eutectic Al-Si) [1], Mg-Al-Zn magnesium alloy (eutectic Mg-β-$Mg_{17}Al_{12}$) [2], pearlitic steel (eutectoid cementite Fe_3C + ferrite) [3] and Ti-6.5wt% Si alloy (eutectic Ti-Ti silicide Ti_5Si_3) [4] and so on. Generally, a eutectic structure can exhibit high strength and high ductility by combining one hard phase and one ductile phase. High-entropy alloys (HEAs) have become a new research frontier in the metallic materials community; they offer a wide range of microstructural tunability from simple single-phase condition to complex eutectic mixtures. As compared to conventional metallic materials, HEAs hold distinct characteristics: (1) high-entropy effect, (2) sluggish diffusion effect, and (3) severe lattice distortion [5]. Single-phase HEAs including face-centered cubic (*fcc*), body-centered cubic (*bcc*), hexagonal close packed (*hcp*), and multi-phase systems including *fcc* + *bcc* phases have been developed [6]. Lu et al. [7] developed a eutectic structured $AlCoCrFeNi_{2.1}$ HEAs or EHEA consisting of *fcc* and B2 phases. In this EHEA, high strength of B2 phase and high ductility of *fcc* phase have been merged together. Similar to $AlCoCrFeNi_{2.1}$, Giwa et al. [8] developed another eutectic HEA system of $Al_{0.7}CoCrFeNi$. A previous work by the authors [9] showed that $Al_{0.7}CoCrFeNi$ exhibits a

dual phase of *fcc* and B2 (B2 with *bcc* nano-precipitates), and the alloy strength can be further enhanced via annealing at low temperature by the formation of coherent nano-scale $L1_2$ precipitates in the *fcc* phase.

Understanding fundamental mechanism of high strain rate (dynamic) deformation in metallic materials is critical to designing impact-tolerant structures used in automobile, aerospace and defense applications [10]. Dynamic deformation often results in strain localization causing adiabatic shear band (ASB) formation. The thermal softening during ASB formation can lead to premature failure of the component [11]. Therefore, a detailed investigation of the microstructural evolution of ASB in metallic materials before and after impact loading tests is desirable [12, 13]. Hat-shaped specimens, commonly referred to as top hat specimens, have been widely used to study the dynamic deformation behavior under shear loading [14-24] using split-Hopkinson pressure bar (SHPB) apparatus. This sample geometry promotes shear localization resulting in deformation focused in a narrow shear band (~ 2–50 μm wide). Inside the shear bands, dynamically recrystallized grains of the order of 20–300 nm in diameter are observed [20], which can exhibit a shear texture. Observation of a rather wide zone with increasing rotation and elongation of the grains shows a rather abrupt transition from relatively homogeneous shear. Several important conclusions have been drawn from SHPB tests on hat-shaped specimens of various conventional materials:

(1) three stages exist during SHPB tests of hat-shaped specimens, namely: (i) onset of strain localization, (ii) ASB formation, and (iii) micro-cracks initiation and propagation [14]. The width of the shear band is narrowed down along the shear direction from top to bottom [15], and its width affects the homogeneity of stress and deformation in the shear bands [14]. There is increased recrystallization with strain, which increases from the edge of the shear band and reaches a maximum at the center.

(2) Dynamic recrystallization (DRX) is observed in most the tested materials including copper [16], steel [17, 18], pure titanium [15], titanium alloys [14, 18], and aluminum alloy [19]. The shear texture is also observed in low-nickel-containing steel [17], pure titanium [15], and nickel alloy [20]. The DRX is confirmed by the emergence of ultra-fined grains with low dislocation density within the shear band [17]. Meyer et al. showed the effect of temperature on shear band width and extend of dynamic recrystallization in copper [16]. The room temperature shear band microstructure is rather broad (~300 μm) and its thickness is reduced to ~50 μm at 523 K [16]. Wang et al. showed that the grain boundaries in the shear band are geometrical necessary boundaries with high-angles. The temperature in the shear band is about 943 K which is high enough to meet the thermal needs of recrystallization.

(3) Twinning played an important part in dynamic deformation [15] in medium and low stacking fault energy alloys such as CoCrNi (medium entropy alloy, MEA) and $Al_{0.3}$CoCrFeNi (HEA). Excellent strain hardening in $Al_{0.3}$CoCrFeNi led the authors to report an absence of ASB after SHPB tests of hat-shaped specimens [21].

(4) The geometry of the specimen is key in restricting the deformation mode to shear. The major principal stress σ_1 is compressive first. The evolution of hydrostatic stress from compressive to tensile is dictated by the ratio r1/r2 (top radius and bottom radius, refer Figure 1). The overlap between the top and bottom dictates how much the material is under compression initially before it undergoes shear. Peirs et al. showed that the lesser the ratio r1/r2 is from one (the outer diameter of the hat is larger than the inner diameter of the hole in the brim) the higher the force needed to deform the specimen [14]. When r1/r2= 0.975, the shear stress is homogeneous. When r1/r2 is smaller, hydrostatic pressure is much more important. For very small ratio r1/r2 the

experiment is closer to a compression test than a shear test. For specimens with r1/r2 > 0.975, the hydrostatic stress is lower, but the shear stress is less homogeneous along the shear line. Consequently, the calculated average shear stress is not representative for actual shear stress in the center of the shear zone. A specimen with the outer diameter of the hat slightly larger than the inner diameter of the brim is the best compromise between good homogeneity of the shear stress, measurability of the shear stress and a stress state as close as possible to pure shear.

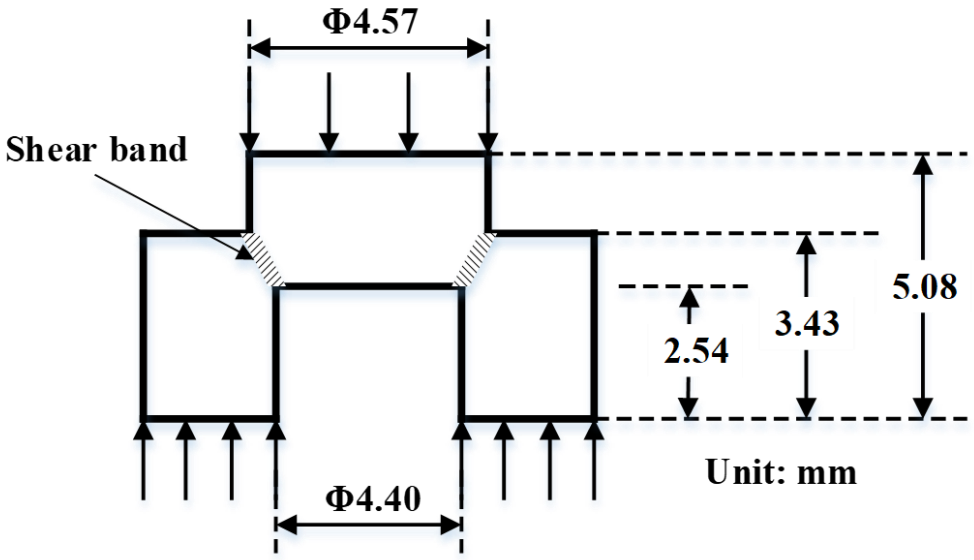

Figure 1. schematic showing the dimensions of the hat shaped specimen used for shear testing under dynamic.

Current work is the first investigation of shear deformation of eutectic HEAs (EHEAs) and effect of precipitation strengthening on the formation of ASBs in any alloy. We investigated two heat treated sample conditions of the EHEA and compared their deformation response under shear loading. After a low-temperature heat treatment at 580 °C, the *fcc* phase in the lamellar two-phase microstructure is strengthened by formation of ordered $L1_2$ nano-precipitates, without compromising the tensile ductility of the alloy. We used gun pressures ranging from 10 psi to 40 psi to shoot the Kolsky bar in the SHPB apparatus resulting in increasing displacement rate (velocity of deformation). The width of the ASB increased as the gun pressure was increased. The precipitation of $L1_2$ phase did not delay the formation of ASB or affect the ASB width, however, the deformed region around ASB, consisting of profuse twinning in *fcc* phase, was reduced from 80 μm to 20 μm in the stronger precipitation strengthened condition. Nano-indentation results showed the change in hardness of the *fcc* and B2 phases before and after deformation and variation of hardness across the ASB.

2. Experimental section

The $Al_{0.7}CoCrFeNi$ alloy (15 at.% Al and 21.25 at.% each of Co, Cr, Fe, Ni) was arc-melted. The ingot was remelted five times for homogenization of the alloy, inverting it after each melt. The as-cast alloy was homogenized at 1150°C for 1 h to annihilate the dislocations and reduce micro-segregations from casting process to assist in cold deformation of the alloy. The alloy was then rolled at room temperature to 30% reduction in thickness. Subsequent annealing at 1100°C for 5 mins was done to homogenize and recrystallize the alloy at high temperature. The cold-rolled and homogenized condition is referred to as ***HTA (high temperature annealed)*** hereafter. Another low-temperature annealing treatment was done at 580°C for 24 h on the HTA condition to precipitate a fine-scale distribution of $L1_2$ phase inside *fcc* lamellae, this is referred to as the ***HTA-580*** condition. In

all the heating steps, the samples were placed in the furnace after the set temperature was reached and cooled by water quenching after a specified treatment time.

The microstructural examination was carried using a scanning electron microscope (SEM) including electron backscatter diffraction (EBSD) and transmission electron microscope (TEM). Microstructural characterization was performed using FEI Nova-NanoSEM 230™ coupled with energy dispersive spectroscopy (EDS). Conventional TEM studies were carried out with an FEI Tecnai G2 TF20™ operating at 200 kV. Precipitate characterization was done using conventional and high angle annular dark field-scanning TEM (HAADF-STEM) modes. TEM foils were prepared by an FEI Nova Nanolab 200 dual-beam focused ion beam (FIB) instrument using a Ga ion beam for milling. The ion beam thinning of the samples was done in multiple steps starting from 30 kV ions and finishing with 5 kV ions to reduce the surface damage caused by higher energy ions. Samples were subjected to quasi-static tensile test using the mini tensile testing machine at a strain rate of 1×10^{-3} s^{-1} and dynamic deformation using a SHPB apparatus. An emitter working pressure range of 10-40 psi was used to obtain different deformation rates. The dimensional details of the hat-shaped specimen is presented in the results section in Figure 1. *HTA was tested with 20, 30 and 40 psi and HTA-580 was tested with 10 and 20 psi gun pressures. The different gun pressure correspond to different striker bar velocity i.e. 10 psi – 7 m/s, 20 psi – 11.26 m/s, 30 psi – 14 m/s, and 40 psi – 17.1m/s. Different gun pressures were used to assess the effect of deformation rate whereas constant gun pressure of 20 psi on HTA and HTA-580 was used to evaluate the influence of precipitation strengthening on shear deformation.* Vickers hardness test was performed on the samples using a load of 500 g load for 10 s at regular intervals in a straight line across the shear band. Nano-indentation experiments were performed using TI-Premier Triboindenter (Bruker, Minneapolis, MN, USA) with a diamond Berkovich tip across the deformed and un-deformed regions at a maximum load of 1000 μN. For each indent, the load was linearly increased to 1000 μN in 0.25 s, held constant for 0.25 s, and unloaded in 0.25 s. A spacing of 100 nm was maintained between neighboring indents to avoid overlap of their plastic zones.

3. Results and Discussion

3.1. Thermal aging for precipitation strengthening

$Al_{0.7}$CoCrFeNi consists of the lamellar eutectic structure of *fcc* and B2/*bcc* phases (Figure 2). The SEM microstructure from the HTA condition is shown in Figure 2(a). The backscattered electron diffraction (BSED) image in Figure 2 (a) shows a two-phase eutectic type of microstructure with a bright contrast phase and dark contrast phase organized in the lamellar arrangement. TEM was used to identify the crystal structure and the composition of the two lamellae. Figure 2 (b) shows the selected area diffraction patterns (SADPs) from the two phases. The SADPs was taken from the bright region in the SEM image was consistently indexed to be from *fcc* phase aligned in [011] zone axis, while the dark region was indexed as *bcc* phase consisting of ordered regions. The $[001]_{B2/bcc}$ zone axis is shown in Figure 2 (b, lower part). The presence of extra-super lattice spots in (001) positions in the SADP from $[001]_{B2/bcc}$ zone axis clearly establish the ordering of this phase. The STEM results showed that the *fcc* phase is enriched in Co, Cr and Fe and B2/*bcc* phase are enriched in Al and Ni (Figure 2 (c)) marked with yellow and white arrows respectively in the figure. A detailed high-resolution examination of B2 lamellae showed that it consists of fine-scale precipitation of Cr rich *bcc* phase within it (Supplementary Figure 1). As this B2+*bcc* phase is consistent in both the heat treatment conditions is not a variable in our study, we would call B2+*bcc* lamellae as B2 lamellae. The second sample condition (HTA-580) was obtained by heat treating the HTA condition further at 580 °C for 24h as depicted by the schematic in Figure 2 (d). HTA-580 condition induced nano-scale $L1_2$ precipitates in *fcc* lamellae. The change in Al distribution in HTA and HTA-580 as examined by EDS mapping and the SADP from $[111]_{fcc}$ in HTA-580 in Figure 2 (d) verify the presence of ordered nano-scale $L1_2$ phase in HTA-580. EDS results of HTA and HTA-580 constituting elemental maps of all elements are shown in Supplementary Figure 2 and 3.

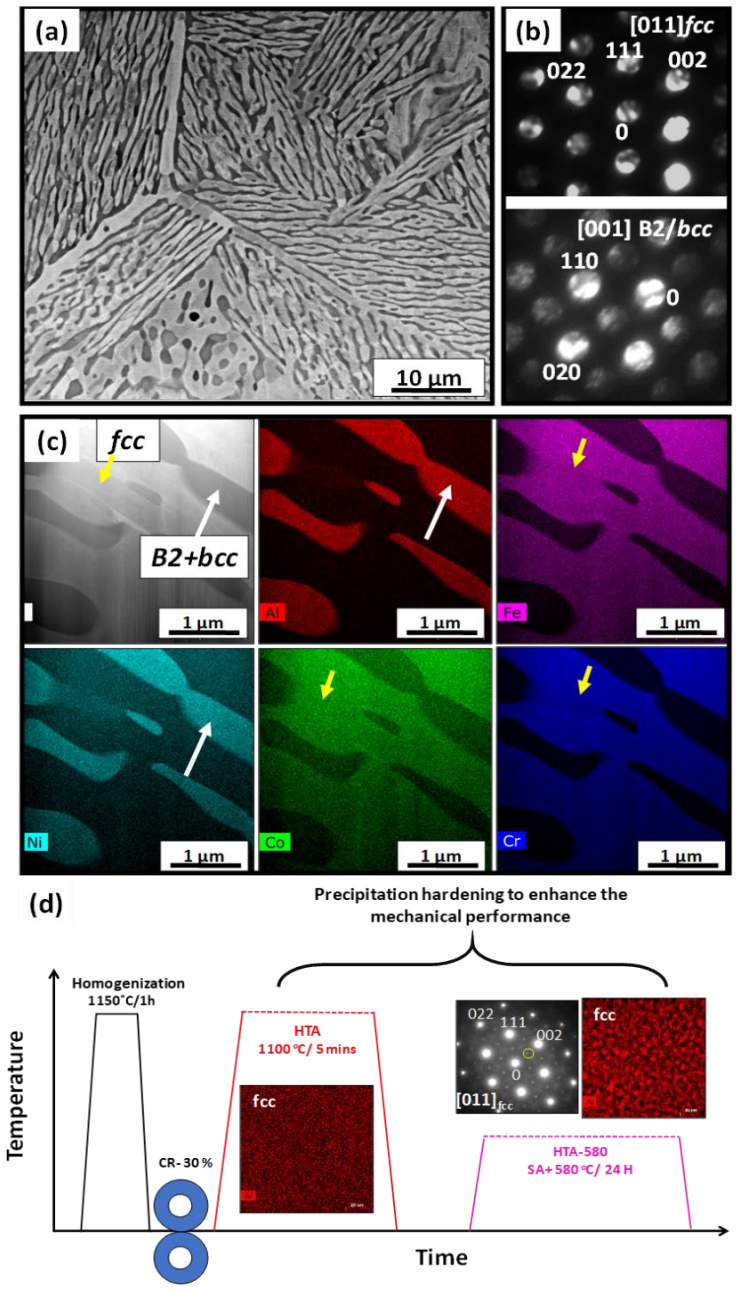

Figure 2. *SEM results*: (a) SEM of HTA condition of $Al_{0.7}CoCrFeNi$ alloy; *TEM results*: (b) diffraction pattern of *fcc* and B2/*bcc* phase; (c) EDS maps of various elements showing the compositional distribution within the microstructure. Note that *fcc* phases (labelled by a yellow arrow in (c)) is enriched in Fe, Cr and Co and B2/*bcc* phases (labelled by a white arrow in (c)) is enriched in Al and Ni; and (d) schematic of thermo-mechanical treatment to obtain the two different microstructures and high magnification STEM EDS map of Al showing the presence of $L1_2$ precipitates in *fcc* after second heat treatment.

3.2. Mechanical properties

3.2.1. Quasi-static tensile test

Quasi-static tensile testing of both the heat-treated conditions was performed to evaluate the change in mechanical performance due to precipitation of the ordered $L1_2$ phase under uniaxial loading. Quasi-static tensile testing displayed that strength of $Al_{0.7}CoCrFeNi$ in HTA-580 condition increased compared to $Al_{0.7}CoCrFeNi$ in HTA condition (Figure 3 (a)). The *fcc*+$L1_2$/*bcc*+B2 microstructure (HTA-580) in this alloy exhibited a tensile yield strength (YS) close to 1000 MPa (~990

Preprints (www.preprints.org) | NOT PEER-REVIEWED | Posted: 10 March 2020 doi:10.20944/preprints202003.0154.v1

Peer-reviewed version available at Entropy 2020, 22, 431; doi:10.3390/e22040431

MPa), ultimate tensile strength (UTS) ~ 1400 MPa and elongation to failure of ~13% while the *fcc*/*bcc*+B2 microstructure in HTA condition showed a YS of 780 MPa, UTS of ~1100 MPa and elongation to failure of 17% under quasi-static loading (strain rate of 10^{-3}). The YS increased by 200 MPa which can be attributed to the $L1_2$ precipitates in *fcc* lamellae formed after the low-temperature heat treatment at 580°C. A detailed microstructural examination of post deformed condition after tensile testing can be accessed elsewhere [9].

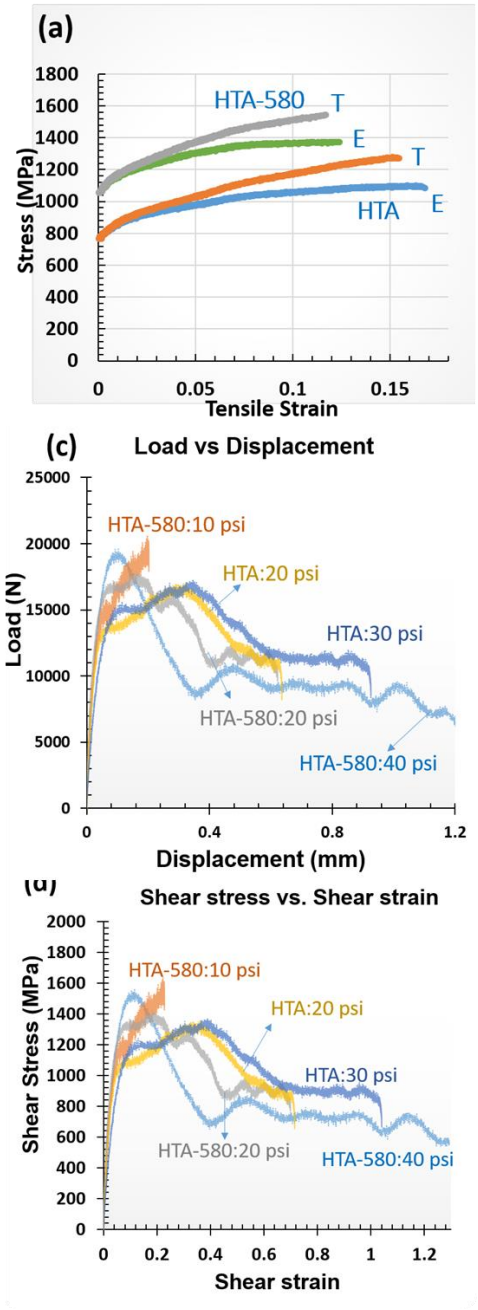

Figure 3. (a) Quasi-static tensile curves showing the engineering (E) and true (T) stress-strain behavior of HTA and HTA-580 condition; (b and c) load vs displacement, and estimated shear stress vs shear strain curves under dynamic compression loading of hat-shaped specimens deformed at different velocities.

3.2.2. Dynamic shear compression of top hat specimen

In the current work we also examine the two heat treatment alloy conditions under a localized shear deformation by using hat shaped specimens. The dimensions of the samples are shown in

Figure 3 (b). Kolsky bar or SHPB with gun pressure ranging from 10 psi to 40 psi was used to conduct the tests. Gun pressure directly related to deformation velocities ranging from 1.6 m/s (10 psi) to 2.3 m/s (40 psi). Load versus displacement curves for the two heat treatment conditions viz. HTA (*fcc* and B2+bcc) and HTA-580 (*fcc*+$L1_2$ and B2+bcc) are shown in Figure 3 (c). The shear stress is estimated by dividing the load by deformed area [$\pi*(h_2-h_1) * (r_1+r_2)$] and shear strain is estimated by dividing displacement by width (h_2-h_1) and are plotted in Figure 2(d). The flow stresses increase for lower strains as the alloy work hardens, a sudden drop in the flow stress signifies the formation of ASB. Figures 3 (c and d) show the test results from HTA-580 tested with 10 psi and 20 psi pressure and HTA tested with 20 psi, 30 psi and 40 psi gun pressure. The drop in the flow stress is not seen in the 10 psi condition as the net strain is not sufficient to cause the formation of ASB and resulting thermal softening. In all the other conditions we observe a sudden drop in the flow stress which corresponds to the observation of ASB and thermal softening (to be discussed in the next section). Dynamic Recrystallization accompanied in the process causes pronounced local softening of the material, while being driven by mechanical strain rather than temperature [24]. Gun pressure of 40 psi resulted in the fracture of the specimen. Note, that different gun pressure leads to the different velocity of deformation (deformation rate) resulting in variable displacement from the initial shape.

3.2.3. Microscopic analysis of the shear region in the deformed hat shaped specimen

Figure 4 shows the BSED SEM images of the deformed hat shaped specimen from the two conditions (HTA and HTA-580) loaded under different gun pressures. Figures 3 (a and d) show the SEM images of the cross-section of HTA-580 samples loaded under 10 and 20 psi pressure, respectively, while Figures 4 (b, c, and e) present the deformed region from HTA samples loaded under 20 and 30 psi. Note that in Figures 4 (a)) no adiabatic shear band is seen as the gun pressure (deformation rate) was insufficient to result in the formation of a shear band. As we increased the gun pressure to 20 psi (Figures 4 (b, c, and d), we formation of ASBs. A low magnification SEM image of the cross-section is shown in Figure 4 (b). The photograph of the cross-section of a deformed hat shaped specimen is shown as an inset and the location of the SEM examination is highlighted by a red circle. The yellow arrows in Figure 4 (b) show the low magnification image of the ASB formed in HTA:20psi condition. On examining the ASB at high magnification as shown in Figure 4 (c), we can note that the width of ASB is ~4 μm for this sample and deformation condition (HTA:20psi). Figures 4 (d) show the BSED image from the HTA-580 deformed with 20 psi pressure. The width of the ASB in HTA-580:20 psi is very similar (~4 μm) to the width of ASB in HTA:20psi (Figures 4 (c) and (d)) deformed specimen suggesting no clear influence of precipitation strengthening ASB formation. However, the width of ASB increased to ~10 μm in HTA:30psi deformed specimen, which suggests a direct correlation with the deformation rate. Higher deformation rate increased the width of ASB but precipitation strengthening did not have a noticeable influence. In most materials the shear band width (Δ) scaled with $\Delta = \sqrt{(KT/(\sigma*\varepsilon))}$ [25]. In our case the shear band width at the onset of localization is similar between the two specimens despite one being stronger than the other. This relationship being known to hold for many materials; however, it may not hold for the case where the length scale of microstructure variations approaches the estimated shear band width. There is insufficient experimental result from the eutectic microstructures on formation of ASBs to conclusively comment on this observation.

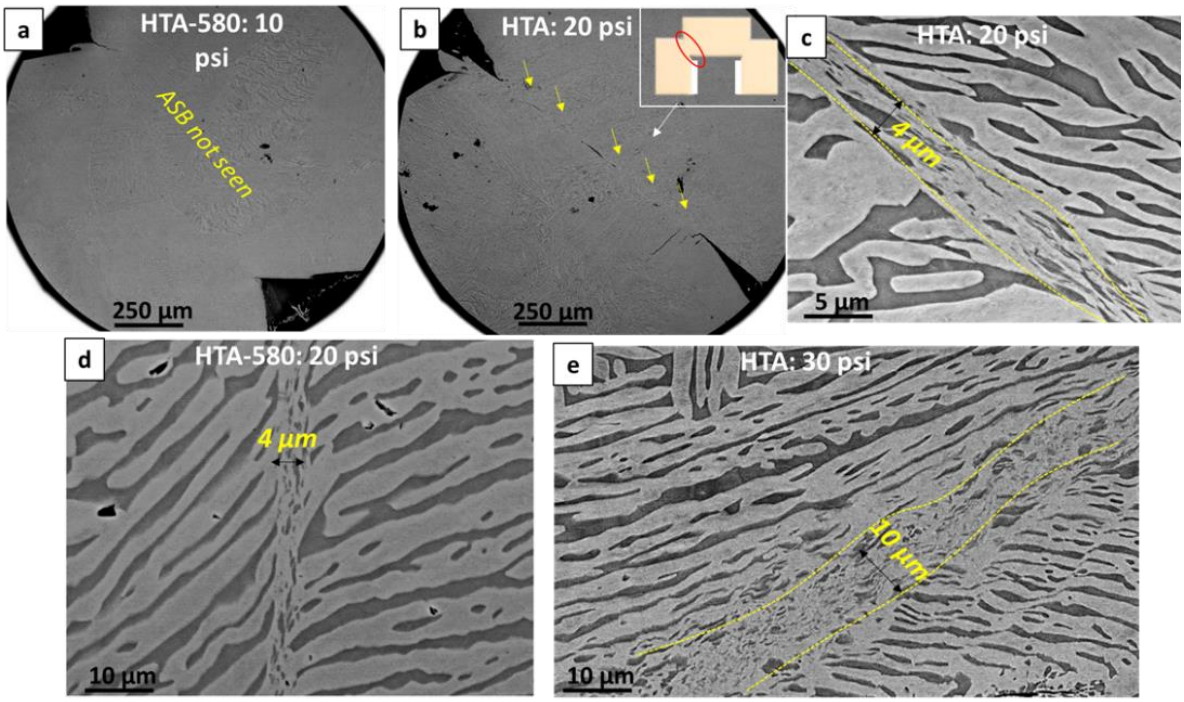

Figure 4. SEM images showing deformed hat-shaped specimen. (a) HTA-580 deformed with 10 psi gun pressure, no ASB is observed. (b) HTA deformed using 20 psi, the yellow arrows show the location of cracking and ASB formation. (c) high magnification image of the HTA-20 psi condition showing the width of the ABS to be about 4 µm. (d) HTA-580:20psi condition (e)) HTA:30psi condition where a 10 µm wide ABS can be seen in the center.

Further analysis of deformed specimens with electron backscattered diffraction (EBSD) orientation image microscopy (OIM) shows that the width of extended deformed region is much larger than the width of ASB observed in the SEM (Figure 5). The inverse pole figures (IPFs) overlaid with confidence index (CI) and the phase maps overlaid with CI from the different samples and deformation conditions are shown in Figure 5. Low CI is suggestive of highly deformed structure and hence the width of the highly deformed region is estimated here based on the width of dark contrast (low CI) region in the figure. Figure 5 (a-d) show the IPF+CI and phase map + CI from HTA-580:10psi, HTA-580:20psi, HTA:20psi, HTA:30psi conditions, respectively. Each of the figures has a photograph of the sample cross-section highlighting the region of interest. HTA-580:10psi did not show any region of low CI which is consistent with SEM images where no ASB formation was observed. The strain hardened and region undergoing plastic deformation around the ASBs are ~80, 20 and 150 µm wide for HTA:20psi, HTA-580:20psi and HTA-580:30 psi, respectively, in the deformed specimens. Note, HTA:20 psi and HTA-580:20 psi specimens showed a similar ASB width on SEM-BSED imaging, but the deformed region was much lower for HTA-580:20 psi specimen. Hence, even though the width of ASB only depended on the deformation rate, HTA-580 condition having stronger *fcc* phase that is strengthened by coherent $L1_2$ precipitates, needed high flow stresses to deform compared to HTA condition. We will now show a detailed TEM examination of the ASBs and the deformed region around it.

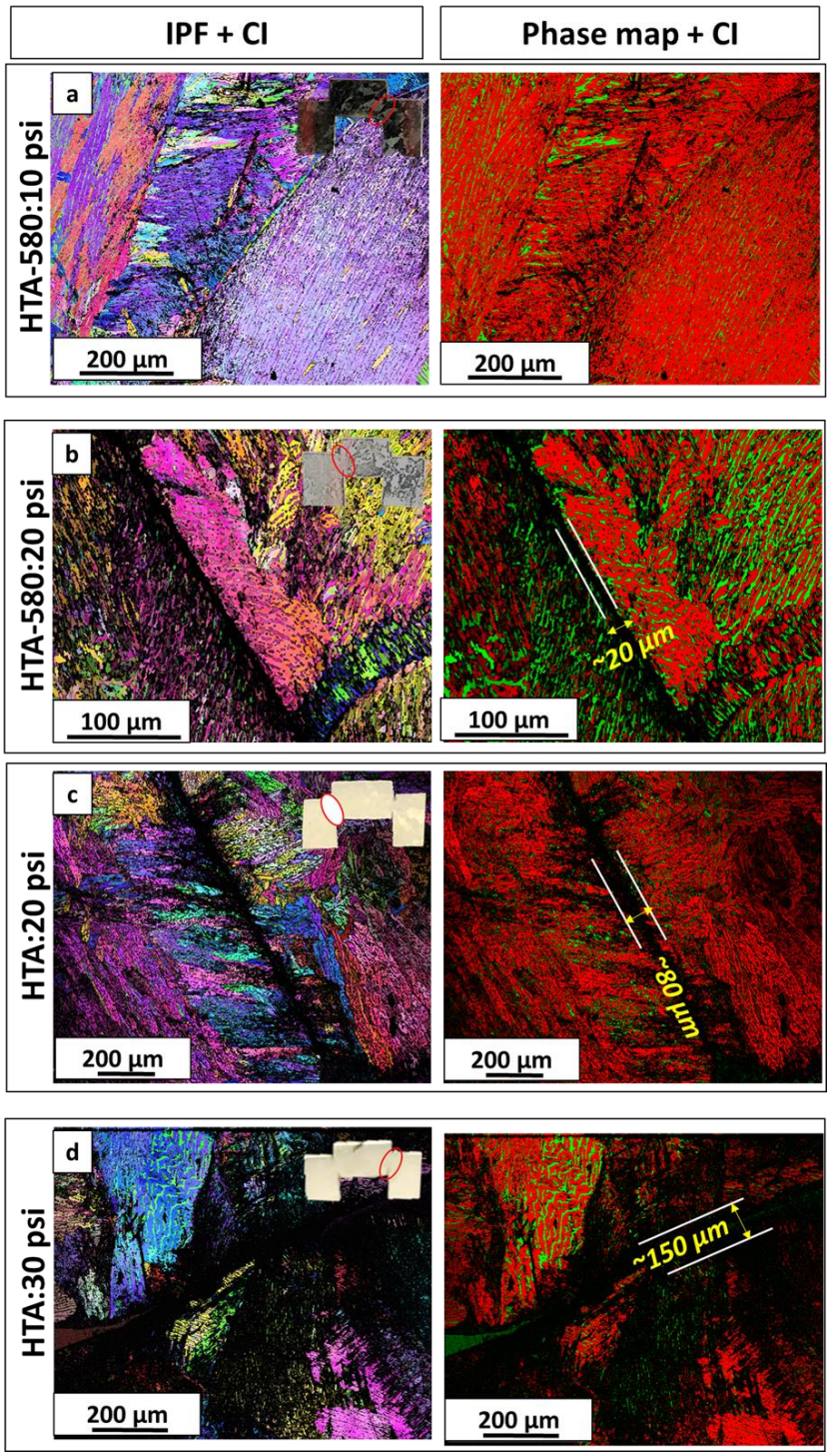

Figure 5. EBSD IPF and phase map of deformed hat-shaped specimens. (a) IPF and phase map from HTA-580:10psi. (b)) IPF and phase map from HTA-580:20psi. (c)IPF and phase map from HTA:20psi. (d)IPF and phase map from HTA:30psi.

Figure 6 shows the TEM results from the ASB formed in HTA-580 samples deformed by using 20 psi gun pressure. Figure 6 (a) shows the SEM image highlighting the location of the TEM lift out. The ASB is marked by a yellow boundary and a bulging in the eutectic lamellae is observed near the ASB due to plastic deformation. A montage of STEM images showing the overall TEM foil is shown in Figure 6 (b). We have selected three regions for further analysis in TEM highlighted by red, blue and yellow color boxes in Figure5 (b). STEM image and EDS maps from the region highlighted by a red box which traverses across the boundary of the shear band are shown in Figure 6 (c). Note, that

even though we see the fragmentation of the lamellae (highlighted by a yellow color arrow in Al map in the figure) at some places but the compositional heterogeneity is maintained even within the ASB. Edwards et al. studied the shear deformation using hat shaped specimen on a 2024 Al alloy [19]. They showed that the high-temperature generated with the formation of ASB caused the second phase particles to coalesce and resulted in a slightly smoother dissolution surface on the particles. The smaller particles aligning in the shear flow direction are suggested as fragmentation of second phase particles inside the ASB leading to the formation of the rigid walls of the shear band. EDS of the larger second phase particles showed their composition to be different from that of the matrix material [19]. In the current work on examining the region outside the ASB as shown in Figure 6(d), we notice that the $L1_2$ phase within fcc has disordered and the presence of high density of nano-twins. The BFTEM image in the figure shows a high amount of dislocation density in the region. An SADP pattern from $[011]_{fcc}$ is shown as the inset on left of the figure, superlattice spots corresponding to the $L1_2$ phase are not seen suggesting deformation induced disordering of the matrix. Disordering of $L1_2$ due to deformation has been reported earlier after tensile and compression tests as well [9]. The inset on the right of the figure shows the high magnification BFTEM image highlighting the deformation twins. Earlier Kuang et al. found {10–12} < –1011 > tensile and {11–22} < 11 2-3> compressive two types of twins in the deformation region around the shear band in pure Ti after dynamic impact loading [15].

On examining within the ASB we notice nano-structuring of the grains. From Figure 6 (e), dynamically recrystallized grains of the size scale of 100-200 nm can be noted. One such grain has been highlighted by the yellow color boundary in the figure. A higher magnification image and the SADP from this region are shown as the insets, further ascertaining nano-structuring of the grains within the ASB. At high strain rates ($>10^3$ s^{-1}), the deformation process is extremely fast and can be considered as an adiabatic process. The temperature inside an ASB is a function of shear strain [22, 23]. Meyer et al. showed that the temperature can be ~1000 K in SS304 at a shear strain of 40% [22]. Yang et al. estimated the temperature in pure Ti to be around 1073 K on explosive loading with strain rate of 10^6/s [23]. The width of shear band in Yang et al. study was 4-8 μm, however, Piers et al. showed that the width depends heavily on the sample geometry and dimensions [14].

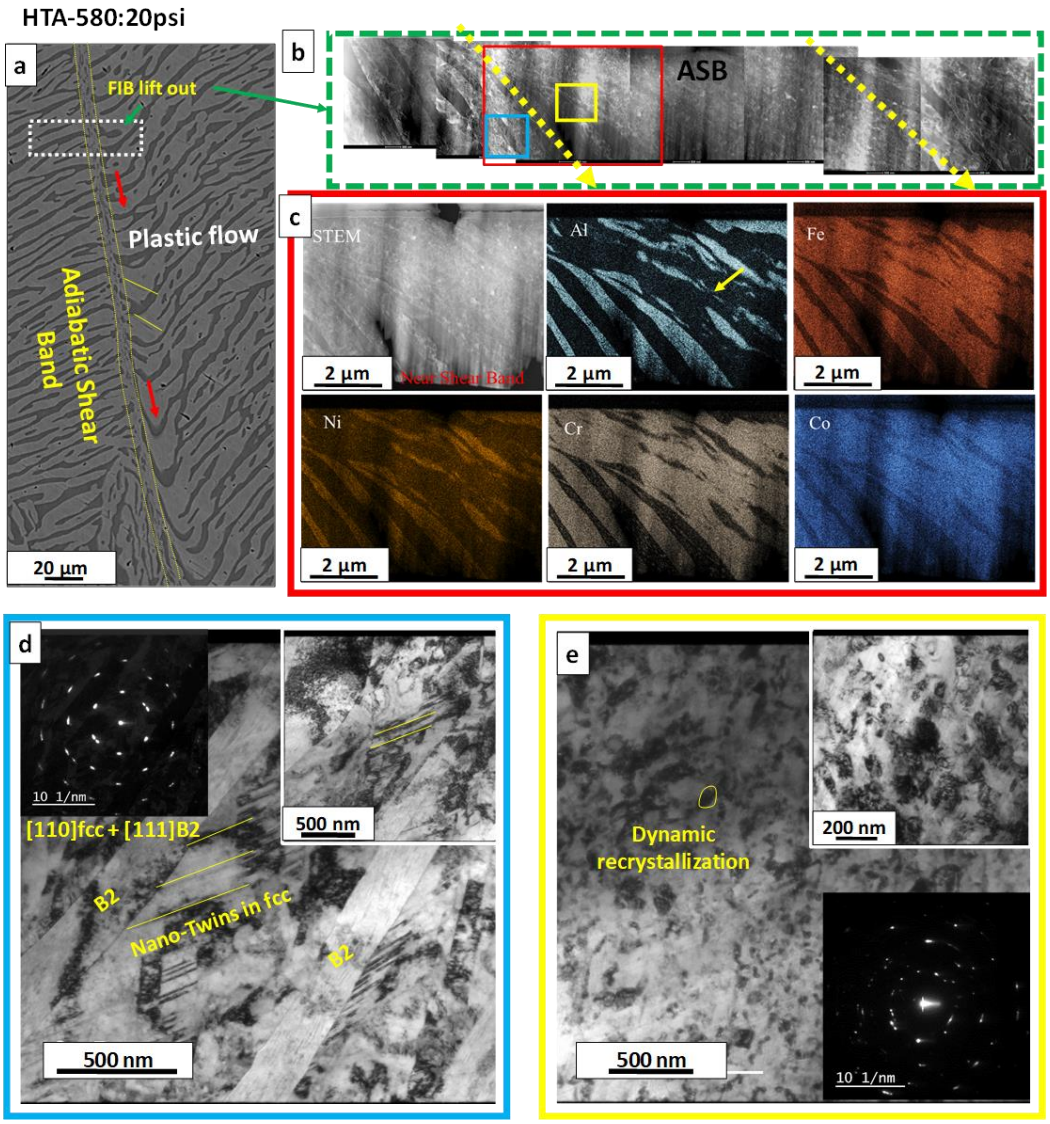

Figure 6. Microstructural analysis on adiabatic shear band in HTA-580:20psi deformed specimen. (a) shows the SEM images highlighting the location of the TEM lift out; (b-e) show the TEM results; (b) shows the STEM image of the TEM foil traversing across the ASB; (c) EDS maps from the region highlighted by red rectangle in (b); (d) BFTEM and the SADP from the blue square in (b). This region is just outside the ASB. Note the profuse number of nano-twins and high dislocation density in this region; (e) The region inside the ASB marked by yellow box in (b). The BFTEM and SADP from this region are shown here. Dynamic recrystallization is observed within the ASB. .

Temperature rise in the shear band associated with the deformation plays a significant role in the study of microstructure mechanism and is estimated by the following equation [22, 23]:

$$T = T_0 + \frac{\eta}{\rho C_v}\int_{\varepsilon_s}^{\varepsilon_e} \sigma d\varepsilon \qquad (1)$$

where T_0 is the initial deformation temperature, η is the fraction of plastic energy converted to heat (generally ~90%), ρ is the mass density, C_v is the heat capacity, σ is the stress and ε is the strain. For $Al_{0.7}CoCrFeNi$ in this study, T_0 = 293 K, ρ is.7080 kg/m^3, C_v = 476 J/kg·K the T can be estimated to be in range of 500 K to 800 K (melting point of the alloy is around 1550 K). Meyer et al. simulated the recrystallization mechanism within a shear band assuming T=0.5T_m. They suggested that the recrystallization happens by grain boundary rotation and limited reorientation. The time taken for the deformation at the strain rate of 10^3/s in the present study is in the order of a few µsecs. The observation of dynamically recrystallized grains suggest temperature reaching >0.5T_m. The localized

mechanical response of the individual phases due to shear deformation was evaluated using nano-indentation as detailed below.

3.2.4. Estimation of instability strain from culver criterion

To predict the strain at which the adibadic shear band forms, Culver proposed a simple condition for a mechanical instability to begin to form [26, 27]. Assuming a pure shear deformation, τ (shear stress) does not increase with γ (shear strain) or $d\tau/d\gamma = 0$, when we reach the instability strain. Culver derived a simple relation for predicting the instability strain (modified by et al) $\gamma_i = n\rho C/(d\tau/dT)$ at constant strain rate. γ_i is the instability strain, n is strain hardening coefficient, ρ the density of the alloy, C is the specific heat capacity, and T is the temperature. The estimation of $d\tau/dT$ is not very straightforward and requires a large number of isothermal experiments. Such a data is rarely available for most alloys. However, this equation implies that a material with large strain hardening coefficient n, should need high instability strain. The value of n and K are measured using the power-law dependency of stress-strain ($\sigma = K\gamma^n$). The value of K is 1512 for HTA and 1638 for HTA-580 condition, and n is 0.549 for HTA and 0.512 for HTA-580 (refer supplementary Figure 5). The density of the $Al_{0.7}CoCrFeNi$ alloy is estimated to be ~7300kg/m^3 [28] and due to lack of data C is assumed to be equal to SS304 (500J/kg/°C). The value of $(d\tau/dT)$ for 304 steel has been reported to be ~2000 KPa/K [26, 27]. Based on these assumption instability strains is roughly estimated to be 1for HTA and 0.93 for HTA-580. The experimentally observed value are 0.41 for HTA and 0.4 for HTA-580. The instability strain increases is observed to increase n, however, Culver criteria overestimates the values by a factor of more than 2. Such an over estimation was also reported by Walley [26] for titanium alloy. More experimental results are needed to accurately predict the instability strain for the current alloy.

3.2.5. Microhardness testing and Nanoindentation details

Microhardness measurements were done on samples HTA:20psi, HTA-580:10 psi, HTA-580:20psi and HTA-580:30 psi using a standard Vickers microhardness tester. The indents were spaced at regular intervals of 160- 200 μm in a straight line covering approximately 2-3 mm distance as shown in Figure 7. The indent on the shear bands in sample served as a fiducial marker for nano-indents which were performed later in the same region. It was observed that the base hardness in HTA condition is around ~300 Hv while the hardness of HTA-580 sample varied in the range of 370-400 Hv. A hardness vs distance plot is shown in Figure 7 on traversing across the sheared region as shown in the figure by an arrow. An average of three readings was used to plot the curve; it is seen that in all deformation conditions an increase in hardness is seen in the neck region of the top hat specimen where the ASB is formed after deformation. This is due to the strain hardening effects. There a plausible softening effect caused by adiabatic temperature rise inside ASB which was probed using nanoindentation. The width of the spike in hardness in the curves also gives an approximate distance range of plastic deformation in each condition. The spike is broadest in HTA:30psi and narrowest in HTA:10psi, which is expected. However, this width is much larger as compared to that noticed on SEM and EBSD characterization.

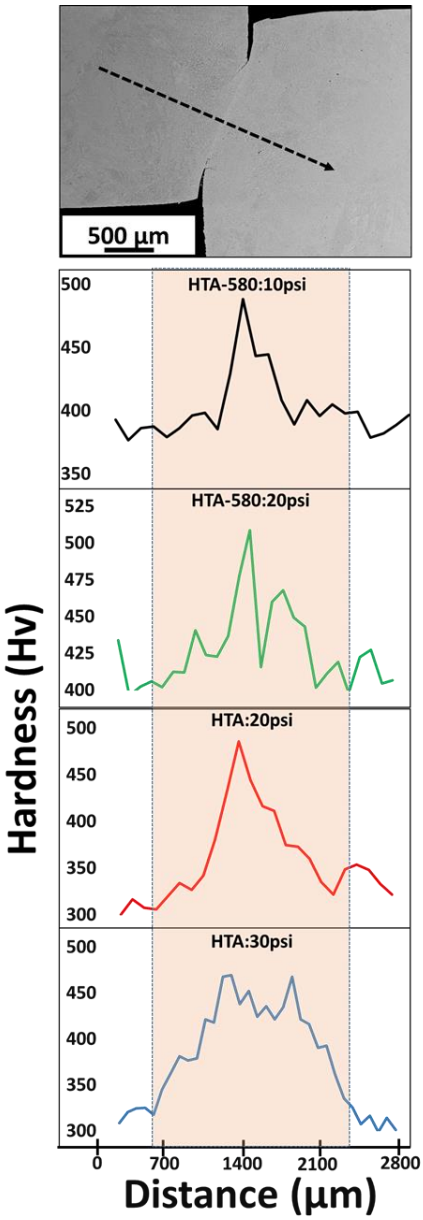

Figure 7. Vickers Hardness profile and results for samples under study. Top to bottom- location of indentations, results from HTA-580:10psi, HTA-580:20psi, HTA-20 psi, HTA:30psi conditions respectively.

Nano-indentation tests were performed using the standard Berkovich tip at the load of 1000 µN to compare the effect of individual phases before and after deformation. Nanoindentation maps of 30 µm × 14 µm were made on the deformed and undeformed region for three top hat samples, namely HTA:20psi, HTA-580:20psi and HTA:58030psi. Figure 8(a) depicts the map for base material where no deformation was seen. Figure 8(b) shows the deformed region maps covering the shear band and its surrounding plastic region. The black region is the B2 phase while the white region is the *fcc* phase. A high magnification image covering FCC, B2 phase and ASB is shown in Figure 8 (c). The nano-indents on B2 and *fcc* phases were identified and approximately 50 indents from the B2 phase and 100 indents from the *fcc* phase were taken for average calculations. Table 1 summarizes the nano-indentation results for various sample conditions. The sample is divided into three regions for characterization viz. in base (away from ASB), near ASB (5-50 µm away from ASB) and within ASB.

The base hardness of *fcc* phase in HTA sample was 4.1 to 4.2 GPa and that in HTA-580 sample was 5.2 GPa. The base hardness of the B2 phase in HTA sample was 6-6.1 GPa whereas in HTA-580

Preprints (www.preprints.org) | NOT PEER-REVIEWED | Posted: 10 March 2020 doi:10.20944/preprints202003.0154.v1

Peer-reviewed version available at Entropy 2020, 22, 431; doi:10.3390/e22040431

sample was 6.9 GPa. The hardness of *fcc* and B2 phase decreased in both HTA and HTA-580 conditions in near ASB region after 20 psi deformation but it increased for 30 psi deformation. The reason for this trend is unclear. The hardness within ASB was in the range of 3.4-3.7 GPa in HTA and HTA-580 conditions after 20 psi whereas 5.9 GPa in HTA condition after 30 psi deformation. Vicker's hardness test which is a bulk method showed a clear trend of increase in hardness ongoing from base to deformed region, however, such a trend is not observed in nanoindentation. The anomalous trend in the nano-hardness cannot be explained at this point and needs further study to understand and will be explored in the future. Lastly, we present the microstructural characterization of the failed sample deformed at 40 psi.

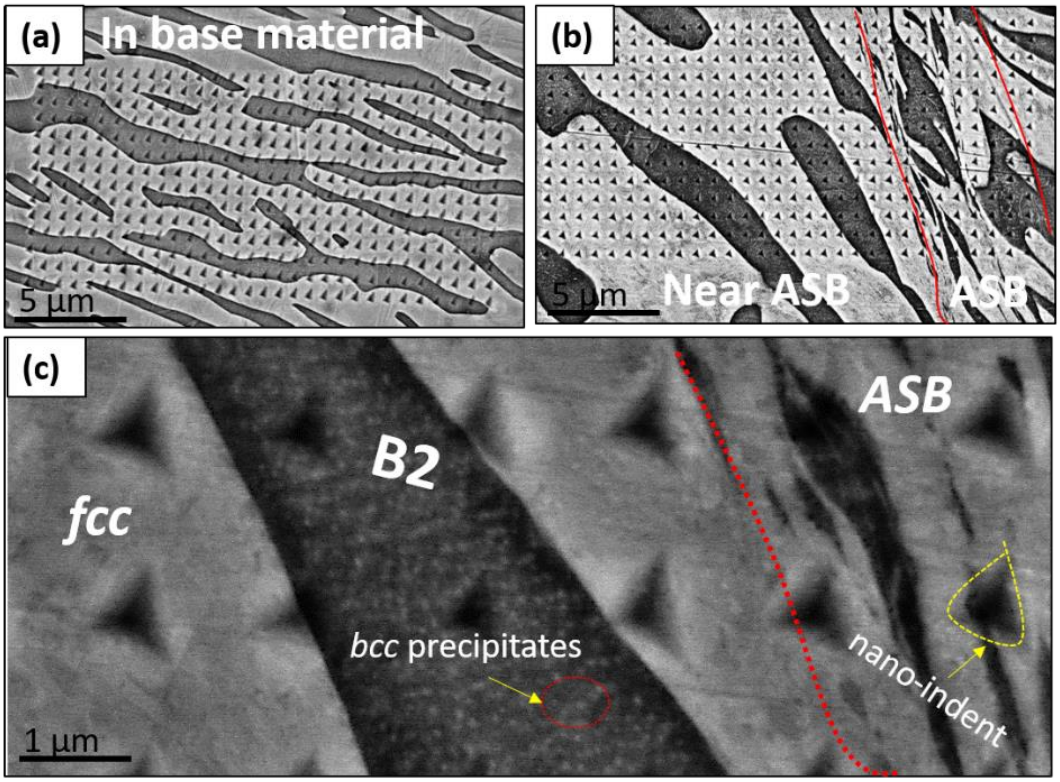

Nano indentation Hardness (GPa)					
Sample Condition	FCC		B2		In ASB
	Base	Near ASB	Base	Near ASB	
HTA: 20 psi	4.1±0.4	3.5±1.1	6.0±0.4	4.1±1.2	3.4±1.1
HTA-580: 20 psi	5.2±0.4	4.4±0.2	7.9±0.8	5.6±0.4	3.7±0.4
HTA-30 psi	4.2±0.4	5.2±0.7	6.0±0.4	6.5±1.0	5.9±1.1

Figure 8. Nanoindentation maps for (a) Base material of Top Hat specimen (b) Map depicting the undeformed, near ASB and ASB. (c) High magnification image near shear band showing *fcc* and B2 phases.Table showing the results of nanoindentation for HTA:20psi, HTA-580:20 psi and HTA 580:30psi. All hardness values are in GPa.

3.2.6. Microscopic analysis of the fractured hat-shaped specimen

Peer-reviewed version available at Entropy 2020, 22, 431; doi:10.3390/e22040431

Fractured HTA:40 psi specimen shows that the B2 phase is fractured and the SEM examination suggested localized melting of the B2 phase and recrystallization of *fcc* grains (Figure 9 and Supplementary Figure 4). Figure 9 (a) shows the photograph of the fractured sample where a yellow color box marks the region of interest. Figure 9 (b) is an SEM-BSED image showing multiple shear bands and EBSD analysis from specific regions marked with white boxes shown in Figures 9(c-e). The IPF and phase maps from each of these regions show that the B2 phase lamellae are fractured and partially melted. Figure 9 (e) clearly shows a highly recrystallized *fcc* grain structure with equiaxed grains and presence of annealing twins. Figure 9 (f) and Supplementary Figure 4 shows that the cracking is limited to the B2 phase and broadening of cracks is seen to accommodate the plastic flow. The temperature estimated by Equation 1 comes out to be ~800 K, however melting of B2 phase suggests localized temperatures reaching around ~1300 K (based on the simulated phase diagram shown in [9]) on loading at 40 psi. Hence, Equation 1 can be underestimating the temperature reached during ASB formation.

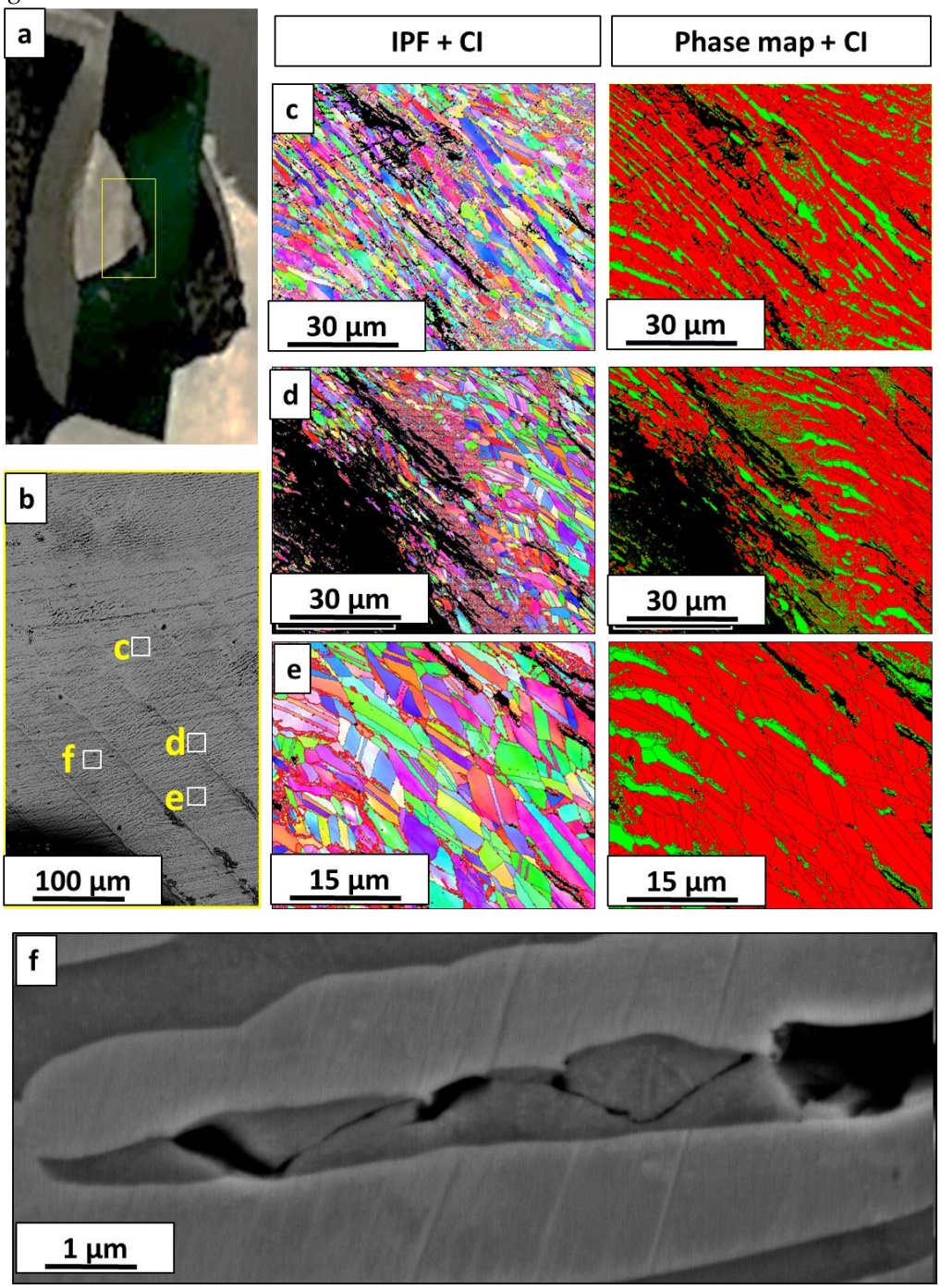

Figure 9. Microstructural analysis on fractured HTA:40psi specimen.

4.Conclusions

Dynamic shear response of a eutectic HEA ($Al_{0.7}$CoCrFeNi) was investigated via mechanical and microstructural characterization. Hat shaped specimen geometry was used to understand the effect of shear localization in this alloy. A benchmark alloy condition (HTA) consisting of *fcc* and B2+bcc lamellae were compared with the HTA-580 condition consisting *fcc*+$L1_2$ and B2+bcc lamellae. Aging at 580°C for 24 h resulted in the formation of nano-scale $L1_2$ precipitates in *fcc* lamellae providing precipitation strengthening to the alloy. Dynamic shear testing of the two heat treatment conditions was conducted using a split Hopkinson's pressure bar apparatus at different deformation rates. The two conditions were characterized in detail before and after the dynamic shear loading to comparison of the effect of precipitation strengthening and deformation rate.

The major finding of the paper is summarized as follow:

(1) The tensile yield strength (quasi-static testing at 10^{-3}/sec) of the $Al_{0.7}$CoCrFeNi eutectic HEA in HTA condition was 780 MPa which increased to 990 MPa after precipitation of $L1_2$ phase in the HTA-580 condition. Such an increase in mechanical properties was noted in nanoindentation response of individual phases (*fcc* and B2) in the HTA-580 condition.

(2) The shear deformation tests were conducted using variable gun pressures resulting in different deformation rates in the SHPB apparatus. The HTA-580 condition was tested under 10 psi and 20 psi loading conditions and the HTA condition was tested under 20 psi, 30 psi, and 40 psi loading conditions. The 10 psi loading rate (1.6m/s) was insufficient to cause the formation of ASB whereas the loading rate of 40 psi (2.3 m/s) resulted in the fracture of the specimen. The 20 psi loading rate has been used to compare the deformation in the HTA vs HTA-580 conditions.

(3) Formation of ASBs led to a sudden decrease in flow stresses for both HTA and HTA-580 conditions, due to the thermal softening accompanied by dynamic recrystallization within the ASBs. Although the width of ASB in HTA:20psi and HTA-580:20psi were observed to be similar (~4 μm), the plastically deformed region around the ASB was much less for HTA-580:20 psi specimen.

(4) The adiabatic shear localization occurs at low strains for the high strength material, and the eutectic microstructure does not delay cracking. The precipitation of $L1_2$ phase in *fcc* increased the tensile strength of the alloy. However, no significant change was observed on formation of ASBs. however, higher strength material (precipitation strengthened condition) has narrower extend of deformation zone, thus narrower strain hardening region.

(5) A high density of nano-twins was observed in the region around the ASB which may be responsible for strain hardening of the alloy before ABS formation. The nano-structuring within ABS suggests dynamic recrystallization and thermal softening. A local temperature of ~800 K is estimated to have reached during testing for a few μsec causing the recrystallization in the ASBs which are adiabatically restricted in diffusion and heat flow.

(6) The microstructural characterization of the fractured specimen suggested the formation of multiple ASBs and local melting of the B2 phase and cracking limited within B2 phase. Pronounced recrystallization in the *fcc* phase consisting of equiaxed *fcc* grain with annealing twins is also noted. The lamellar structure seems to be broken in the region close to the fracture.

(7) Microhardness testing across the shear band showed a ~20-30 % increase in the hardness values ongoing from the base microstructure to the region deformed while shear banding. Nanoindentation was used to characterize individual lamellae before and after deformation. The trend in both *fcc* and B2 phase before and after deformation are inconclusive and needs further analysis. However, the hardness within the ASBs is noted to drop in all specimen.

Acknowledgments: The work was performed under cooperative agreement between Army Research Laboratory and University of North Texas (W911NF-16-2-0189). We also acknowledge Materials Research Facility at the University of North Texas for microscopy facilities.

Conflicts of Interest: The authors declare no conflict of interest.

Data Availability: Data will we available with the corresponding authors and can be accessed on a reasonable request.

References

1. Ma, Z.Y., Sharma, S.R. and Mishra, R.S., 2006. Effect of friction stir processing on the microstructure of cast A356 aluminum. Materials Science and Engineering: A, 433(1-2), pp.269-278.
2. Feng, A.H. and Ma, Z.Y., 2007. Enhanced mechanical properties of Mg–Al–Zn cast alloy via friction stir processing. Scripta materialia, 56(5), pp.397-400.
3. Raabe, D., Choi, P.P., Li, Y., Kostka, A., Sauvage, X., Lecouturier, F., Hono, K., Kirchheim, R., Pippan, R. and Embury, D., 2010. Metallic composites processed via extreme deformation: Toward the limits of strength in bulk materials. MRS bulletin, 35(12), pp.982-991.
4. Saha, R.L., Nandy, T.K., Misra, R.D.K. and Jacob, K.T., 1991. Microstructural changes induced by ternary additions in a hypo-eutectic titanium-silicon alloy. Journal of materials science, 26(10), pp.2637-2644.
5. Tsai, M.H. and Yeh, J.W., 2014. High-entropy alloys: a critical review. Materials Research Letters, 2(3), pp.107-123.
6. Miracle, D.B. and Senkov, O.N., 2017. A critical review of high entropy alloys and related concepts. Acta Materialia, 122, pp.448-511.
7. Lu, Y., Dong, Y., Guo, S., Jiang, L., Kang, H., Wang, T., Wen, B., Wang, Z., Jie, J., Cao, Z. and Ruan, H., 2014. A promising new class of high-temperature alloys: eutectic high-entropy alloys. Scientific reports, 4, p.6200.
8. Giwa, A.M., Liaw, P.K., Dahmen, K.A. and Greer, J.R., 2016. Microstructure and small-scale size effects in plasticity of individual phases of Al 0.7 CoCrFeNi High Entropy alloy. Extreme Mechanics Letters, 8, pp.220-228.
9. Gwalani, Bharat, Sindhura Gangireddy, Yufeng Zheng, Vishal Soni, Rajiv S. Mishra, and Rajarshi Banerjee. "Influence of ordered L1 2 precipitation on strain-rate dependent mechanical behavior in a eutectic high entropy alloy." Scientific reports 9, no. 1 (2019): 6371.
10. Zener, C. and Hollomon, J.H., 1944. Effect of strain rate upon plastic flow of steel. Journal of Applied physics, 15(1), pp.22-32.
11. Wei, Q., Kecskes, L., Jiao, T., Hartwig, K.T., Ramesh, K.T. and Ma, E., 2004. Adiabatic shear banding in ultrafine-grained Fe processed by severe plastic deformation. Acta materialia, 52(7), pp.1859-1869.
12. Xue, Q., Gray, G.T., Henrie, B.L., Maloy, S.A. and Chen, S.R., 2005. Influence of shock prestraining on the formation of shear localization in 304 stainless steel. Metallurgical and Materials Transactions A, 36(6), pp.1471-1486.
13. Yuan, F., Jiang, P. and Wu, X., 2012. Annealing effect on the evolution of adiabatic shear band under dynamic shear loading in ultra-fine-grained iron. International Journal of Impact Engineering, 50, pp.1-8.
14. Peirs, J., Verleysen, P., Degrieck, J. and Coghe, F., 2010. The use of hat-shaped specimens to study the high strain rate shear behaviour of Ti–6Al–4V. International Journal of Impact Engineering, 37(6), pp.703-714.
15. Kuang, L., Chen, Z., Jiang, Y., Wang, Z., Wang, R. and Liu, C., 2017. Adiabatic shear behaviors in rolled and annealed pure titanium subjected to dynamic impact loading. Materials Science and Engineering: A, 685, pp.95-106.
16. Andrade, U., Meyers, M.A., Vecchio, K.S. and Chokshi, A.H., 1994. Dynamic recrystallization in high-strain, high-strain-rate plastic deformation of copper. Acta metallurgica et materialia, 42(9), pp.3183-3195.
17. Wang, B.F., Liu, Z.L., Wang, X.Y. and Li, Z.Z., 2014. An EBSD investigation on deformation-induced shear bands in a low nickel austenitic stainless steel under controlled shock-loading conditions. Materials Science and Engineering: A, 610, pp.301-308.
18. Meyer, L.W., Staskewitsch, E. and Burblies, A., 1994. Adiabatic shear failure under biaxial dynamic compression/shear loading. Mechanics of Materials, 17(2-3), pp.203-214.
19. Edwards, N.J., Song, W., Cimpoeru, S.J., Ruan, D., Lu, G. and Herzig, N., 2018. Mechanical and microstructural properties of 2024-T351 aluminium using a hat-shaped specimen at high strain rates. Materials Science and Engineering: A, 720, pp.203-213.
20. Johansson, J., Persson, C., Lai, H. and Colliander, M.H., 2016. Microstructural examination of shear localisation during high strain rate deformation of alloy 718. Materials Science and Engineering: A, 662, pp.363-372.
21. Li, Z., Zhao, S., Diao, H., Liaw, P.K. and Meyers, M.A., 2017. High-velocity deformation of Al 0. 3 CoCrFeNi high-entropy alloy: Remarkable resistance to shear failure. Scientific Reports, 7, p.42742.
22. Meyers, M.A., Xu, Y.B., Xue, Q., Perez-Prado, M.T. and McNelley, T.R., 2003. Microstructural evolution in adiabatic shear localization in stainless steel. Acta Materialia, 51(5), pp.1307-1325.

23. Yang, Y., Xinming, Z., Zhenghua, L. and Qingyun, L., 1996. Adiabatic shear band on the titanium side in the Ti/mild steel explosive cladding interface. Acta materialia, 44(2), pp.561-565.
24. Rittel, D., and Z. G. Wang. "Thermo-mechanical aspects of adiabatic shear failure of AM50 and Ti6Al4V alloys." Mechanics of materials 40, no. 8 (2008): 629-635.
25. Dodd, B., and Yilong Bai. "Width of adiabatic shear bands formed under combined stresses." Materials science and technology 5.6 (1989): 557-559.
26. Walley, S. M. "Shear localization: a historical overview." Metallurgical and materials transactions A 38, no. 11 (2007): 2629-2654.
27. Staker, M.R., 1981. The relation between adiabatic shear instability strain and material properties. Acta Metallurgica, 29(4), pp.683-689.
28. Gorsse, S., Nguyen, M.H., Senkov, O.N. and Miracle, D.B., 2018. Database on the mechanical properties of high entropy alloys and complex concentrated alloys. Data in brief, 21, pp.2664-2678.